Theoretical Raman spectrum and anharmonicity of tetrahedral OH defects in hydrous forsterite

Etienne Balan, Marc Blanchard, Michele Lazzeri, Jannick Ingrin

Theoretical Raman spectrum and anharmonicity of tetrahedral OH defects in hydrous forsterite

Etienne Balan[1], Marc Blanchard[1], Michele Lazzeri[1], Jannick Ingrin[2]

[1] Institut de Minéralogie, de Physique des Matériaux, et de Cosmochimie (IMPMC),

Sorbonne Universités, UPMC Univ Paris 06, UMR CNRS 7590, Muséum National d'Histoire

Naturelle, UMR IRD 206, 4 place Jussieu, F-75005 Paris, France

[2] UMET, UMR CNRS 8207, Université de Lille1, Bât. C6, 59655 Villeneuve d'Ascq, France

Corresponding author:

Prof. Etienne Balan

Institut de Minéralogie, de Physique des Matériaux, et de Cosmochimie (IMPMC), Sorbonne

Universités, UPMC Univ Paris 06, UMR CNRS 7590, Muséum National d'Histoire Naturelle,

UMR IRD 206, 4 place Jussieu, F-75005 Paris, France

Email: Etienne.Balan@impmc.upmc.fr

52

Abstract: Substitutional mechanisms involving hydrogen incorporation at vacant tetrahedral sites play a major role in water incorporation in olivine. IR absorption spectra of hydrous forsterite samples usually display a cluster of narrow and weakly anharmonic OH stretching bands at wavenumbers above 3500 cm^{-1}. A broader absorption band displaying pronounced temperature-dependent shift and broadening is often superimposed to this diagnostic spectrum and was tentatively assigned to interstitial OH groups. A less frequently observed band with similar temperature-dependent characteristics is related to a coupled incorporation of hydrogen and boron at the tetrahedral site. Here, we re-examine these interpretations by computing the theoretical Raman spectrum and investigating the local vibrational properties of OH groups at the tetrahedral site of forsterite. The present results show that the two anharmonic bands are both ascribed to the protonated O2 site in the clumped $(B,H)_{Si}^{x}$ and the $(4H)_{Si}^{x}$ defects. The peculiar orientation of the corresponding OH groups does not allow H-bond sharing and leads to efficient vibrational phase relaxation of the stretching mode through a hindered rotational mode coupled to the vibrational density of states of the host. The occurrence of interstitial OH groups previously proposed to interpret specific anharmonic bands of the forsterite IR spectrum is highly challenged by this new explanation. These results confirm that at high pressure and high temperature, hydrogen incorporation in forsterite is essentially dominated by $(4H)_{Si}^{x}$ defects.

Key-words: forsterite; OH defects; IR spectroscopy; Raman spectroscopy; ab initio calculations; anharmonicity.

74

1. Introduction

77

78   Olivine, $(Mg,Fe)_2SiO_4$, is able to incorporate minor amounts of hydrogen as OH-

79   bearing defects in its crystal structure (Beran & Zemman, 1969; Wilkins & Sabine, 1973;

80   Beran & Putnis, 1983). As it is the most abundant rock-forming silicate in the upper mantle,

81   these defects are expected to significantly contribute to the global budget of water in Earth

82   (*e.g.*, Bell & Rossman, 1992; Bolfan-Casanova, 2005; Demouchy & Bolfan-Casanova, 2016).

83   The related modifications of the mechanisms of plastic crystal deformation might also play an

84   important role in plate tectonics and mantle dynamics (*e.g.*, Chopra & Paterson, 1984;

85   Mackwell *et al.*, 1985; Mei *et al.*, 2000; Demouchy *et al.*, 2012; Tasaka *et al.*, 2015).

86   Accordingly, the hydrogen solubility in olivine has been investigated as a function of a

87   number of thermodynamic parameters relevant to mantle conditions (typically T=1700 K and

88   P=10 GPa), including temperature, pressure, water activity, silica activity, and oxygen

89   fugacity (e.g. Bai & Kohlstedt, 1993; Mosenfelder *et al.*, 2006; Smyth *et al.*, 2006; Grant *et*

90   *al.*, 2007; Withers *et al.*, 2012; Férot & Bolfan-Casanova, 2012). However, the variability of

91   incorporation mechanisms and location of OH groups in the olivine structure as revealed by

92   the infrared spectrum of natural samples (Libowitzky & Beran, 1995; Matsyuk & Langer,

93   2004; Koch-Muller *et al.*, 2006; Beran & Libowitzky, 2006; Matveev & Stachel, 2009; Gose

94   *et al.*, 2010) is still poorly understood.

95   Thermodynamic laws inferred from early measurements of water solubility in olivine

96   were consistent with an incorporation mechanism involving an isovalent substitution of two

97   protons for a divalent magnesium ion (*e.g.*, Kohlstedt *et al.*, 1996), a model theoretically

98   supported by the easier formation of vacancies at Mg sites than at Si sites (Walker *et al.*,

99   2006). However, a dependence of the mechanism of hydrogen incorporation on Si and Mg

100   activity conditions was revealed by infrared spectroscopic observations performed on

101   synthetic and natural olivine (Matveev *et al.*, 2001; 2005) as well as on synthetic forsterite

102   (the Mg end-member of olivine) samples (Lemaire *et al.*, 2004; Berry *et al.*, 2005),

103   questioning the pertinence of the Mg-vacancy model in forsterite and olivine. The relations

104   between the infrared spectrum and the Si and Mg activity conditions, together with the

105   theoretical modeling of the infrared spectroscopic properties of OH defects in forsterite

106   (Balan *et al.*, 2011; Umemoto *et al.*, 2011), consistently point to a dominant incorporation

107   mechanism involving a $(4H)_{Si}^{x}$ defect, i.e. the isovalent substitution of four protons for a

108   tetravalent silicon ion at tetrahedral sites. This mechanism leads to infrared absorption bands

109   typically observed at frequencies above 3400 cm^{-1}; whereas protonated Mg vacancies lead to

110   bands observed between 3100 and 3200 cm^{-1}. Similar high frequency bands are observed in

111   the Raman spectra of synthetic hydrous forsterite samples (Hushur *et al.*, 2009; Bolfan-

112   Casanova *et al.*, 2014). A preferential protonation of Si vacancies in forsterite has also been

113   recently inferred by an NMR study combining the measurement and a theoretical modeling of

114   chemical shift and dipolar coupling parameters (Xue *et al.*, 2016). Finally, a number of

115   absorption bands have been related to the interaction of OH bearing defects and other

116   chemical elements in natural olivine samples and their synthetic counterparts (*e.g.*, Berry *et*

117   *al.*, 2005, 2007; Walker *et al.*, 2007; Crépisson *et al.*, 2014a; Blanchard *et al.*, 2016). The

118   extrapolation of spectroscopic observations made at ambient conditions to temperatures

119   relevant to the Earth upper mantle was however questioned by the in-situ study of Yang &

120   Keppler (2011) who reported the infrared spectrum of hydrated San Carlos olivine recorded

121   up to 1100 °C.

122   Further information on the OH defects in forsterite was obtained by studying the

123   anharmonic behaviour of OH stretching vibrational modes, through the low-temperature

124   dependence of its infrared absorption spectrum (Ingrin *et al.*, 2013). Most of the observed

125 bands previously ascribed to OH incorporated at tetrahedral or octahedral sites displayed a

126 moderately anharmonic behaviour, slightly stronger for the more effectively H-bonded OH

127 groups at octahedral sites. In contrast, a stronger anharmonicity was inferred for two bands

128 (referred to as band 3a and band 8a; Fig. 1a) observed at high frequencies in the investigated

129 sample (3550 and 3598 cm^{-1} at room temperature for bands 3a and 8a, respectively) and

130 displaying marked temperature-dependent frequency shifts and broadenings (Fig. 1). Such

131 anomalous behaviour, distinct from that of the bands ascribed to substitutional OH groups,

132 was interpreted in Balan *et al*. (2014) using the Persson & Ryberg formalism (Persson &

133 Ryberg, 1985a,b): the anharmonic behavior is related to the indirect coupling of the high-

134 frequency vibrational stretching mode to the vibrational density of states (phonon bath) of the

135 crystalline host via a specific low-frequency vibrational mode, referred to as exchange mode.

136 A structural model corresponding to band 3a at 3550 cm^{-1} was proposed in terms of interstitial

137 OH groups. Occurrence of interstitial OH groups in olivine has been previously proposed by

138 Bai and Kohlstedt (1993). Interstitial OH groups are indeed expected to be weakly H-bonded,

139 consistent with a relatively high vibrational frequency, and significantly coupled to specific

140 low-energy vibrations leading to a strong anharmonic behaviour. A more recent spectroscopic

141 study of natural and synthetic samples revealed that the band 8a is related to a coupled

142 incorporation of hydrogen and boron at the tetrahedral site of forsterite (Ingrin *et al*., 2014). In

143 this $(H,B)_{Si}^{x}$ defect, referred to as B_H_1 defect (Ingrin *et al*., 2014), the BO_3 group occupies

144 one face of the tetrahedron, delimited by the O1 and the two symmetric O3 oxygen atoms;

145 whereas the H atom is bonded to the opposite O2 atom and points toward the exterior of the

146 tetrahedron. However, the origin of the anharmonic character of the corresponding stretching

147 band was still unclear. It became also apparent that only three of the four bands predicted for

148 the most stable configuration of protonated Si vacancies $(4H)_{Si}^{x}$, referred to as Si_3 defect

149 (Balan *et al*., 2011) were observed in the low temperature spectra. The band related to the

150 protonation of the O2 atom was systematically lacking. This set of observations thus calls for

151 an in-depth re-examination of the peculiarity of the proton environment at the O2 site in

152 forsterite and related anharmonic behaviour.

153   In the present study, we report a theoretical analysis of the energetic landscape

154 controlling the proton dynamics at the tetrahedral sites of forsterite. We also compute the

155 Raman intensity of the OH-stretching bands related to the Si_3 defect, to bring additional

156 constraints for the interpretation of the measured spectra (Hushur *et al*., 2009, Bolfan-

157 Casanova *et al*., 2014). The obtained results make it possible to reconcile different

158 experimental observations and further support a dominant mechanism of water incorporation

159 in forsterite as OH defects associated to vacant tetrahedral sites.

160

161 **2. Theoretical methods**

162

163   The energy landscape and theoretical spectroscopic properties of the defects are

164 obtained from first-principles calculations based on density functional theory (DFT),

165 that is by solving the equation of quantum mechanics (within certain approximations)

166 without using ad-hoc phenomenological parameterization. This approach is commonly

167 considered as predictive for the systems under consideration. The theoretical approach

168 and convergence parameters are the same as in Balan *et al*. (2011). To summarize,

169 calculations were performed using the generalized gradient approximation (GGA) to the

170 exchange-correlation functional (Perdew *et al*., 1996) with the PWscf code of the Quantum

171 Espresso package (Gianozzi *et al*., 2009; http://www.quantum-espresso.org). Periodic models

172 of OH-bearing forsterite were built by inserting one defect in a 2x1x2 supercell (112 atoms)

173 of forsterite (theoretical primitive cell-parameters: $a = 4.78$ Å, $b = 10.28$ Å, and $c = 6.01$ Å).

174 The equilibrium positions were determined at constant volume by minimizing the forces on

175   atoms to less than 10^{-5} Ry/a.u. (1 Ry=13.6057 eV). The harmonic vibrational modes were

176   calculated at the Brillouin zone center (Γ point), using the linear response theory (Baroni *et*

177   *al*., 2001) as implemented in the PHonon code (Gianozzi *et al*., 2009; http://www.quantum-

178   espresso.org). Potential energy surfaces related to selected hydrogen atoms were obtained by

179   calculating the total energy of the system for a series of finite displacements of the hydrogen

180   from its equilibrium position. The Raman spectrum of the Si_3 defect was computed using

181   the vibrational modes previously determined in Balan *et al*. (2011) and the Raman tensors

182   obtained using the second-order response to density functional theory as exposed in Lazzeri

183   and Mauri (2003).

184

185

186   **3. Results and discussion**

187

188   **3.1 Anharmonic OH-stretching bands in forsterite : Reappraisal of experimental data**

189

190   As previously exposed in Ingrin *et al*. (2013), two OH-stretching bands (bands 3a and

191   8a, Fig. 1a) observed in hydrous forsterite samples display an anharmonic behavior

192   significantly stronger than that observed for other OH bands in the same frequency range (e.g.

193   band 7a, Fig. 1a; the same band as the band at 3612 cm^{-1} of Yang & Keppler (2011)).

194   Importantly, both bands are mostly polarized along Y ([010] axis) and their anharmonic

195   behavior is quite similar. It consists in a significant frequency lowering (Fig. 1b) and band

196   broadening (Fig. 1c) when the temperature increases from 79 to 473 K. This anharmonic

197   behaviour was evaluated by Balan *et al*. (2014) using the Persson & Ryberg model of

198   vibrational phase relaxation (Persson & Ryberg, 1985 a,b). In this model, the high-frequency

199   localized vibrational mode (LVM) of a molecular group is anharmonically coupled to a single

200   so-called "exchange mode" at low frequency. The exchange mode is itself weakly coupled via

201   a friction parameter η to the phonon bath of the host crystal. The following relations describe

202   the temperature-dependence of the frequency shift, $\Delta\Omega = \Omega - \Omega_0$, and contribution to the

203   width, $\Delta\Gamma = \Gamma - \Gamma_0$, of the high-frequency LVM band (here the OH-stretching band):

204

205                $\Delta\Omega = \delta\omega/(\exp(h\omega_{ex}/2\pi kT)-1)$ (1)

206

207   and

208

209            $\Delta\Gamma = 2\ \delta\omega\,(\delta\omega/\eta)\ \exp(h\omega_{ex}/2\pi kT)\ /(\exp(h\omega_{ex}/2\pi kT)-1)^2$ (2)

210

211   where h is the Planck constant, k the Boltzmann constant and T the temperature. The

212   parameters ω_{ex} is the harmonic angular frequency of the exchange mode and $\delta\omega$ describes the

213   coupling between the high-frequency LVM and the exchange mode. A fit of the experimental

214   Ω values as a function of temperature using Eq. 1 leads to a ω_{ex} frequency below 300 cm^{-1} and

215   a $\delta\omega$ parameter of -32 and -52 cm^{-1} for the bands 3a and 8a (Balan *et al.*, 2014). These values

216   are entailed by a significant uncertainty related to the limited temperature range that can be

217   experimentally explored and the significant overlap between experimental bands. A slightly

218   different approach can be used to treat the experimental data, taking into account both the

219   measured frequency and width. The contribution to the shift and width predicted by Eq. 1 and

220   2, respectively, becomes temperature independent and negligible at low temperature ($2\pi kT \ll$

221    $h\omega_{ex}$). A residual temperature-independent contribution to the measured width arises from the

222   spectrometer resolution (1 cm^{-1}, Ingrin *et al.*, 2013) and inhomogeneous broadening.

223   Assuming that the lowest measurement temperature is low enough to correspond to the

224   saturation domain (Fig. 1b), the values of Ω_0 and the temperature-independent contribution to

225   the width (Γ_0) were assumed to be equal to those measured at 79K for the bands 3a and 8a

226   (Table 1). For the other bands, their width at 79 K is very close to the spectrometer resolution

227   and Γ_0 was set to 1 cm^{-1}. Following Dumas *et al*. (1990), the Persson & Ryberg model implies

228   that the logarithm of the quantity $\Delta\Gamma/(\Delta\Omega)^2$ is linearly related to the inverse of temperature:

229

230                         $\Delta\Gamma/(\Delta\Omega)^2 = (2/\eta)\,\exp(h\omega_{ex}/2\pi\,kT)$ (3)

231

232   Accordingly, a linear fit of related experimental data should lead to the values of ω_{ex}

233   and η. 0verall, the two anharmonic bands display a behavior consistent with this model (Fig

234   1d). In contrast, the other bands (4a, 5a and 7a) display a systematic departure from linearity.

235   The linear extrapolation to infinite temperature leads to η values of 137 and 438 cm^{-1} for the

236   bands 3a and 8a, respectively (Table 1). The ω_{ex} values extracted from the slope of the linear

237   fits are 387 and 470 cm^{-1}, respectively. These values of exchange frequencies are significantly

238   higher than those previously proposed in Balan *et al*. (2014) (242 and 270 cm^{-1}, respectively).

239   New fits of experimental OH stretching frequencies (Fig. 1b) were then performed by

240   constraining the ω_{ex} and Ω_0 parameters to the above values, leading to coupling parameters

241   ($\delta\omega$ = -68 and -142 cm^{-1} for band 3a and 8a, respectively) about three times stronger than

242   those obtained by Balan *et al*. (2014). At this stage, the broadening predicted by Eq. 2 is fully

243   determined by the coupling parameters $\delta\omega$, exchange mode frequencies ω_{ex}, friction parameter

244   η and Γ_0 values (Table 1). Comparing with experimental data (Fig. 1c), the new sets of

245   internaly consistent experimental parameters can account for the significant increase in the

246   width of bands 3a and 8a with temperature, even though the agreement between model and

247   experiment is not perfect. The adequation between model and experimental data is affected by

248   the difficulty to extract accurate parameters on overlapping bands as well as by the

249   simplifying assumptions of the model. Note that η is still significantly larger than $|\delta\omega|$, which

250   is roughly consistent with the weak coupling assumption of the Persson & Ryberg model. In

251   contrast, the significantly different behavior of the weakly anharmonic bands (4a, 5a, and 7a)

252   suggests that their temperature-dependance would be poorly described by such phase

253   relaxation mechanism involving a single exchange mode.

254

255   3.2 **Theoretical Raman spectrum and structural interpretation of OH-stretching bands**

256   **in forsterite**

257

258   By investigating the temperature dependence of the infrared absorption bands in the

259   spectrum of boron-bearing synthetic forsterite and natural olivine samples (containing up to

260   230 ppm and 72 wt. ppm of B, respectively), Ingrin *et al*. (2014) brought strong evidences

261   relating the band 8a (at 3598 cm^{-1} in room temperature spectra) to a hydroxyl group

262   associated to a trigonal boron group at the tetrahedral site of olivine. In the corresponding

263   atomic-scale theoretical model (B_H_1; Ingrin *et al*. 2014), the BO_3 group occupies the face

264   of the tetrahedron delimited by the O1 and the two symmetric O3 oxygen atoms (Fig. 2). The

265   H atom is bonded to the opposite O2 vertex and points away from the tetrahedron. Its

266   symmetric environment precludes a H-bond sharing with nearby oxygen atoms. This

267   environment displays a strong similarity with that of the O2 atom in the most stable

268   configuration of a four-fold protonated Si vacancy (referred to as Si_3; Balan *et al*., 2011). In

269   the Si_3 configuration, three OH groups are oriented along the edges of the tetrahedral sites,

270   sharing weak H-bonds with nearby OH groups, whereas the O2-H group points away from the

271   tetrahedron and is not H-bonded (Fig. 2). A comparison between the theoretical Si_3 defect

272   (Balan *et al*., 2011) and experimental (e.g., Lemaire *et al*., 2004; Mosenfelder *et al*., 2006;

273   Smyth *et al*., 2006; Kovács *et al*., 2010) infrared spectra indicates that the experimental bands

274   7a, 5a and 4a, characterized by a weakly anharmonic behaviour and room temperature

275 wavenumbers of 3613, 3579 and 3567 cm^{-1}, are dominantly related to the O1-H stretching

276 and to two modes involving the coupled stretching motion of the O3-H groups, respectively.

277 The Raman spectrum of hydrous forsterite (Hushur *et al.*, 2009; Bolfan-Casanova *et al.*,

278 2014) displays three bands at positions coinciding with that of bands 7a, 5a and 3a of the

279 infrared spectrum (Fig. 3). Strong differences are observed in the relative intensities with a

280 marked decrease of the intensity of band 7a in favour of band 5a. The band 4a is not observed

281 in the Raman spectrum suggesting that its intensity is also very weak. The theoretical Raman

282 spectrum (Fig. 3) correctly reproduces these relative intensity changes, thus supporting the

283 theoretical interpretation given for these three bands. Despite a dominant contribution of the

284 O1-H group, the low intensity of band 7a (calculated at 3592 cm^{-1}) is explained by the

285 coupled stretching motion of O2-H and O3-H groups in opposition of phase with the

286 stretching of the O1-H group. When the O1-H bond elongates the three other OH bonds

287 shorten (Fig. 4). In this case, the polarizability change associated to the vibration mode is

288 minimal. This weakens the Raman intensity of this band, which becomes dominated by a

289 residual (XY) cross-polarization term (Fig. 3). In contrast, the displacement of H atoms

290 located on the O3 oxygens increases the polarization associated to the mode, enhancing its

291 infrared absorption. The intensity of the weak band 4a (calculated at 3520 cm^{-1}), which is

292 polarized along the Z direction, is also related to terms of the Raman tensors involving a

293 cross-polarization because it corresponds to an anti-symmetric stretching motion of O3-H

294 groups with respect to the (XY) symmetry plane (Fig. 4). In contrast, the band 5a (calculated

295 at 3540 cm^{-1}), which dominantly corresponds to a symmetric motion of O3-H groups with a

296 lesser contribution of the O1-H group (Fig. 4), displays the strongest Raman intensity, with a

297 dominant polarization along X. It also displays a significant infrared activity (Balan *et al.*,

298 2011). However, neither the Raman spectra nor the low temperature FTIR spectra (Ingrin *et*

299 *al.*, 2013, 2014) reveal the presence of a weakly anharmonic band matching that theoretically

300 predicted for the O2-H group. Meanwhile, the band 3a appears as being systematically

301 associated with the other bands of the Si_3 defect and is also observed at 3548.4 and 3550

302 cm^{-1} in the Raman spectra of forsterite reported by Huschur *et al.* (2009) and Bolfan-

303 Casanova *et al.* (2014), respectively. Considering this convergent set of observations and the

304 similar polarization and anharmonic properties of bands 3a and 8a, it becomes self-evident

305 that the band 3a corresponds to the O2-H group in the Si_3 configuration of protonated

306 silicon vacancies ($(4H)_{Si}^{x}$). Accordingly, the bands 3a, 4a, 5a and 7a (Ingrin *et al.*, 2013) are

307 all related to the vibration modes reported for this configuration in Balan *et al.* (2011). In this

308 case, the band 3a at 3566 cm^{-1} (at 79 K, Fig. 1a) is observed at a frequency relatively lower

309 than that expected from theory (c.a. 3600 cm^{-1}), a feature that could be linked to the stronger

310 mode anharmonicity. Finally, the weak band at 3480 cm^{-1} in the experimental Raman

311 spectrum is most likely related to a slightly less stable configuration of the $(4H)_{Si}^{x}$ defect

312 (Balan *et al.*, 2011). This structural interpretation of the hydrous forsterite spectrum is

313 consistent with the prevalence of electroneutrality at atomic scale in defective ionic or iono-

314 covalent crystals (Kröger & Vink, 1956; Nakamura & Schmalzried, 1983; Crépisson *et al.*,

315 2014b).

316

317 **3.3 Theoretical analysis of OH group anharmonicity**

318

319   In this part, the contrasted anharmonic behavior exhibited by the O2-H groups in the

320 B_H_1 and Si_3 defects compared to the other OH groups in the Si_3 defect is examined on a

321 theoretical basis. The harmonic vibrational modes of both defects were first determined from

322 the usual approach based on a diagonalization of the zone-center dynamical matrix (Table 3),

323 leading to stretching frequencies consistent with the previous investigations (Balan *et al.*,

324 2011; Ingrin *et al.*, 2014). Then, the anharmonic coupling between (harmonic) vibrational

325 modes can be investigated by considering derivatives of the total energy with respect to

326 atomic displacements with orders higher than quadratic. For example, assuming an

327 anharmonic interaction potential between the modes Q_i of the form $V_{1122}=C_{1122}Q_{LVM}^2Q_{ex}^2$, the

328 parameter $\delta\omega$ is given by the following expression:

329

330 $$\delta\omega = \frac{h\,C_{1122}}{2\pi\,\tilde{m}_{LVM}\,\tilde{m}_{ex}\,\omega_{LVM}\,\omega_{ex}} \qquad\qquad (4)$$

331

332 where ω_{LVM} is the harmonic angular frequency of the LVM and $\tilde{m}_{LVM}$ and $\tilde{m}_{ex}$ are the effective

333 masses of the LVM and exchange mode (note that the $\delta\omega$ values in Balan *et al*. (2014) were

334 underestimated due to a wrong prefactor in the expression of C_{1122}).

335 In order to identify the exchange mode and to explain the strikingly different

336 anharmonic behaviour of the specific OH-stretching bands, we remind that the analysis of

337 measurements suggests that the specific behavior of proton at the O2 site is related to the

338 occurrence of an exchange mode at a frequency in the range 400 - 500 cm^{-1}. The analysis of

339 the vibrational properties of the cell simulated within DFT reveals that the displacement of the

340 H atoms transverse to the stretching direction is indeed associated to vibrations in that

341 frequency range. Unfortunately, the diagonalisation of the dynamical matrix of the full system

342 is not a viable approach to determine the properties of this mode since the transverse H

343 displacement turns out to be coupled to several distinct vibrational normal modes.

344 A more transparent understanding of the physics is obtained by analyzing the local

345 environment of OH groups. Focusing on O2-H and O1-H groups, which are both located on a

346 symmetry plane of the forsterite structure, the potential energy landscape related to

347 displacements of hydrogen atoms around their equilibrium position was built by calculating

348 the total energy of the system on a regular 2D grid of atomic positions (Fig. 5). The

349 coordinates of the displacements were defined in a local orthonormal reference frame. The

350 longitudinal displacements δx are parallel to the OH bond and the transverse displacement δz

351 are defined in the perpendicular plane, along the crystallographic c-axis of the forsterite

352 structure. For δx ranging between -0.4 and +0.4 a_0 ($a_0 = 0.529177 \; 10^{-10}$ m) and δz between -

353 1.2 and +1.2 a_0, the surface corresponding to the B_H_1 model displays a complex shape. The

354 short range O-H repulsion dominates for a longitudinal shortening of the bond whereas the

355 potential is relatively flat in the transverse direction. A very similar potential shape was

356 observed for the O2-H and O1-H groups of the Si_3 defect. Although the differences between

357 the potential energy surfaces are not immediately apparent, a 2D polynomial fit of the

358 surfaces performed on a more restricted displacement range (-0.4 and +0.4 atomic units for

359 both coordinates) revealed significant variations in the quadratic transverse coefficient $(\delta z)^2$

360 (Table 3), which determines the exchange mode frequency. It is very remarkable, that the

361 anharmonic coupling terms, such as the $(\delta x)^2 (\delta z)^2$ one, are very similar for the three OH

362 groups. This finding indicates that the differences of the anharmonic behavior of the three OH

363 groups are not related to a difference of the coupling between the LVMs and the respective

364 exchange modes but only to a difference of the exchange-mode frequencies. Why this change

365 of the frequency of the soft transverse modes should have such a dramatic effect on the

366 anharmonic behavior of the stretching modes cannot be understood solely within the Person

367 & Ryberg model but is related to the specificities of the system under consideration.

368   The difference in the quadratic transverse coefficient is more apparent when

369 considering 1D sections of the potential energy surface performed at coordinates δz=0

370 (longitudinal section) or δx=0 (transverse section) (Fig. 6). For the longitudinal section, the

371 potential is almost identical for the three OH groups. It corresponds to a usual OH stretching

372 potential, with significant cubic and quartic contributions (*e.g.*, Szalay *et al.*, 2002). It is also

373 very close to the potential previously determined at the DFT level for inner-OH groups in

374 phyllosilicates (Balan *et al*., 2007). The weak H-bonding of the O1-H group only has a minor

375 effect on the potential shape, which is consistent with the high-values of the corresponding

376 harmonic stretching frequencies (Table 3). In contrast, the transverse sections reveal a more

377 significant difference in the potential shapes. The O2-H group in the B_H_1 and Si_3 defects

378 displays a very similar potential shape. It is characterized by a comparatively smaller value of

379 the quadratic term $(\delta z)^2$, which amounts to about one half of that determined for the O1-H

380 group. In contrast, the higher quadratic coefficient of the O1-H group reflects the highly

381 directional character of H-bonding (e.g. Wood *et al*., 2009). The harmonic frequencies

382 obtained by only considering the displacement of the H atom in this 1D potential are close to

383 450 cm^{-1} for the O2-H groups and 630 cm^{-1} for the O1-H group (Table 3). The same

384 frequencies within numerical errors are obtained by diagonalizing a partial dynamical matrix

385 restricted to the displacement of the H-atom only. The mean square displacements computed

386 for the corresponding modes (Table 2) however show that the H atoms move significantly

387 away from their equilibrium position, indicating that the harmonic model will only provide an

388 indicative picture of the proton dynamics.

389   Additional insight in the system dynamics can be achieved by extending the partial

390 dynamical matrix to the displacements of the O and H atoms belonging to the OH group. In

391 this case, the vibrational modes can be categorized as one stretching, two hindered rotation

392 and three hindered translations. The approach can also be easily extended to the O3-H groups,

393 which are located in an environment less symmetric than that of the O2-H and O1-H groups.

394 The stretching frequencies are very close to those obtained by diagonalizing the full

395 dynamical matrix, as previously observed (Balan *et al*., 2011). The hindered translation

396 modes are grouped between 270 and 470 cm^{-1}. The hindered rotation modes are observed

397 above 630 cm^{-1} for the O1-H and O3-H groups whereas one of these modes has its frequency

398 significantly lowered for the O2-H groups and is observed close to 500 cm^{-1} (Table 3),

399   consistent with the range expected for the exchange mode. It is thus suggested that a shift

400   from > 630 cm^{-1} to 500 cm^{-1} of this hindered rotation mode dramatically affects the

401   anharmonic properties of the OH groups. The other hindered rotation mode corresponding to

402   the orthogonal transverse displacement of the hydrogen is observed at 868, 881, 814 and 925

403   cm^{-1} for the O2-H (B_H_1 and Si_3 models), O1-H and O3-H groups, respectively. These

404   frequencies do not appear as related to the differences in the anharmonic character of OH

405   groups.

406   Although unexpected, the strong effect of the lowering of one of the hindered rotation

407   modes can be understood by considering the peculiar shape of the vibrational density of states

408   of forsterite. This density of states has been reported from experimental measurements (*e.g.*,

409   Rao *et al.*, 1988) and theoretical modeling (*e.g.*, Li *et al.*, 2007). It displays two regions which

410   are well separated by a gap observed between 620 and 820 cm^{-1}. The forsterite structure does

411   not display vibrational modes occurring between these two frequencies. The higher frequency

412   region is related to the dispersion of the internal Si-O stretching modes whereas the lower

413   region involves the dispersion of both internal SiO$_4$ bending modes and external modes. As a

414   consequence, the lowering of one of the hindered rotation frequency from 630 cm^{-1} to 500 cm$^-$

415   ^{1} is expected to introduce a more efficient coupling between this mode and the forsterite

416   phonon bath (Fig. 7). The peculiar anharmonic behavior of the O2-H groups is thus ascribed

417   to the coupling between the stretching LVM with a transverse hindered rotation mode that

418   efficiently relaxes to the phonon bath of the host. In this case, the relatively higher value of

419   the friction parameter η sustains a description of the anharmonic behavior in the weak

420   coupling limit corresponding to the Persson & Ryberg model. In contrast, the hindered

421   rotation modes of the O1-H and O3-H display similar coupling coefficients with the

422   stretching LVM but are much less efficiently coupled to the phonon bath. In this case, the

423 phase relaxation process of the OH stretching mode could involve its direct coupling to the

424 host phonon bath, a much less efficient process (Budde *et al.*, 2001).

425

426 **4. Crystal-chemical and mineralogical implications**

427

428   The present results improve our understanding of the proton crystal-chemistry in

429 anhydrous minerals and solid materials and might provide a firmer basis to interpret

430 experimental petrology results and their extrapolation to inner-Earth processes.

431   Concerning the first aspect, they reveal an unusual relation between H-bonding and

432 anharmonicity. Isolated and weakly H-bonded OH groups are indeed expected to display a

433 weaker anharmonic character than more strongly H-bonded groups (Libowitzky & Beran,

434 2006). It is well established that stronger H-bonding decreases the stretching potential

435 curvature, decreasing the related stretching frequency, and increases its departure from a

436 parabolic function (Nakamoto et al., 1995, Libowitzky, 1999; Szalay et al., 2002, Balan et al.,

437 2007). A stronger H-bonding is also expected to decrease the lifetime of excited stretching

438 vibrational states, inducing a homogeneous broadening of the band. This relation can be

439 roughly described as follows. Infrared absorption corresponds to a coherent excitation of an

440 ensemble of oscillators. Accordingly, the decay of the excited state can occur either through

441 energy transfer from individual excited states to other vibrational states of the crystal

442 (population relaxation process) or through thermal fluctuations inducing a loss in the phase

443 coherence of the excited state (vibrational phase relaxation) (Bonn et al., 1996; Budde et al.,

444 2001; Martin et al. 2006). For high-energy OH stretching modes, population relaxation is not

445 an efficient process because energy conservation requires a coupling with a large number of

446 the host vibrational states. The observed broadening of OH stretching bands is thus dominated

447 by dephasing processes, which can also occur, at least, through two different mechanisms.

18

448   Increasing the H-bond strength can directly strengthen the stochastic modulation of the

449   stretching vibration of the H-bonded OH group or can enhance the population relaxation of a

450   low frequency exchange mode anharmonically coupled to the OH stretching mode. The two

451   mechanisms have been shown to occur, depending on the specificities of OH group

452   environment (Bonn et al., 1996). According to the present results, the thermal-behaviour of

453   high-frequency anharmonic OH bands in the infrared spectrum of hydrous forsterite can be

454   accounted for by the second mechanism. In this case, the reverse relation observed between

455   H-bonding and band broadening results both from the softening of the transverse motion of H

456   atoms not involved in a directional H-bond and from the specific shape of the forsterite

457   vibrational density of states.

458   As H-bonding usually tends to increase the Born effective charge of the H atom, it

459   leads to a related increase in the mode polarization and infrared absorption coefficient that can

460   be correlated to the lowering of OH stretching frequency (Paterson, 1982; Libowitzky &

461   Rossman, 1997; Balan et al., 2008). This dependance is commonly used to quantify OH

462   defects in nominally anhydrous minerals using infrared spectroscopy (Bell et al., 2003; Koch-

463   Müller & Rhede, 2010; Kovács et al., 2010). In the present case, the longitudinal dynamics of

464   H atoms is similar for the different OH groups investigated and the OH quantification

465   procedure should not be affected. Indeed, it is expected that the absorption coefficient of the

466   anharmonic infrared absorption band will be similar to that inferred for the other bands

467   occurring in the similar frequency range. The peculiar anharmonic behavior observed as a

468   function of temperature is not expected to dramatically affect their absorption coefficient.

469   Moreover, the anharmonic bands 3a and 8a do not reveal any peculiar temperature variation

470   of their integrated area (Ingrin et al., 2013).

471   The present structural interpretation of the infrared and Raman spectrum of OH

472   stretching bands in forsterite relates the bands 3a, 4a, 5a and 7a (Ingrin et al., 2013) to the

473   vibration modes of the same $(4H)_{Si}^{x}$ defect (the previous attempt to relate the band 3a to the

474   presence of interstitial OH groups (Balan et al., 2014) should not be considered any more as

475   the most valid hypothesis). As a consequence, the incorporation of hydrogen at tetrahedral

476   sites appears as the dominant incorporation mechanisms and this mechanism should be

477   included in the thermodynamic models of water solubility in forsterite. The observation of

478   similar defects in iron-bearing systems suggests that this conclusion can be most likely

479   extended to olivine (Blanchard et al., 2016). The implications for the solubility laws of water

480   in forsterite and olivine are discussed in Ingrin et al. (2013) and more recently in Blanchard et

481   al. (2016). Note that given the rarity of natural olivine samples with significant boron

482   concentration, the $(B,H)_{Si}^{x}$ defect is not expected to play any major control in the hydrogen

483   speciation in the Earth upper mantle.

484   Beside the identification of the defects, the determination of the corresponding

485   vibrational modes makes it possible to discuss in more details some of the changes in the

486   infrared spectrum of olivine observed as a function of temperature (Yang & Keppler, 2011).

487   Indeed, the disappearance above 400 °C of the band observed at 3612 cm^{-1} at room

488   temperature (band 7a) has been interpreted as revealing a temperature dependent equilibrium

489   between two different proton sites. The present results show that this band is not related to a

490   single OH group but involves the coupled stretching of the four OH groups of a $(4H)_{Si}^{x}$ defect

491   and, most important, that its infrared and Raman intensities are highly dependent on the

492   coupling scheme. Thus, the behaviour reported by Yang & Keppler (2011) could be simply

493   due to a change in the H-bonding geometry and does not necessarily involve a proton

494   migration between different sites at high-temperature. The nature of the OH defects in

495   quenched samples could correctly reflect the high-temperature mechanism of water

496   dissolution in olivine, as commonly assumed before Yang & Keppler (2011). A high-

497   temperature configurational equilibrium can be expected from the previous identification of

498 several stable configuration of the $(4H)_{Si}^{x}$ defect with small energy differences (Umemoto et

499 al., 2011; Balan et al., 2011). As the multiple configurations of the defect contribute to the

500 system entropy, they could stabilize $(4H)_{Si}^{x}$ defects at high temperature. Further studies

501 would be required to better understand the contrasted relative stability of tetrahedral defects

502 observed between olivine and orthopyroxene (Prechtel & Stalder, 2011). As a matter of fact,

503 the OH bands at high frequencies related to the $(4H)_{Si}^{x}$ defects, including the broad band at

504 3550 cm^{-1} are systematically dominant for olivine or forsterite synthesized in presence of

505 orthopyroxene (see for example, Otsuka & Karato, 2011, Withers et al., 2011, Férot &

506 Bolfan-Casanova, 2012).

507

512

513 **References**

514

515 Bai, Q. &Kohlstedt, D.L. (1993): Effects of chemical environment on the solubility and

516   incorporation mechanism for hydrogen in olivine. *Phys. Chem. Minerals*, **19**, 460-

517   471.

518 Balan, E., Lazzeri, M., Delattre, S., Meheut, M., Refson, K., Winkler, B. (2007):

519   Anharmonicity of inner-OH stretching modes in hydrous phyllosilicates: Assessment

520   from first-principles frozen-phonon calculations. *Phys. Chem. Minerals*, **34**, 621-625.

521   Balan, E., Refson, K., Blanchard, M., Delattre, S., Lazzeri, M., Ingrin, J., Mauri, F., Wright,

522   K., Winkler, B. (2008): Theoretical infrared absorption coefficient of OH groups in

523   minerals. *Am. Mineral.*, **93**, 950-953.

524   Balan, E., Ingrin, J., Delattre, S., Kovacs, I., Blanchard, M. (2011): Theoretical infrared

525   spectrum of OH-defects in forsterite. *Eur. J. Mineral.*, **23**, 285-292.

526   Balan, E., Blanchard, M., Lazzeri M., Ingrin, J. (2014): Contribution of interstitial OH groups

527   to the incorporation of water in forsterite. *Phys. Chem. Minerals*, **41**, 105-114.

528   Baroni, S., de Gironcoli, S., Dal Corso, A., Giannozzi, P. (2001): Phonons and related crystal

529   properties from density-functional perturbation theory. *Rev. Modern Phys.*, **73**, 515-

530   561.

531   Bell, D.R. & Rossman, G.R (1992): Water in earth's mantle: the role of nominally anhydrous

532   minerals. *Science*, **255**, 1391–1397.

533   Bell, D.R., Rossman, G.R., Maldener, J., Endisch, D., Rauch, F. (2003): Hydroxide in olivine:

534   A quantitative determination of the absolute amount and calibration of the IR spectrum.

535   *J. Geophys. Res.*, **108**, B2, 2105-2113.

536   Beran, A. & Zemman, J. (1969): Über OH-gruppen in Olivin. *Öster. Akad. Wiss.*, **3**, 73-74.

537   Beran, A. & Putnis, A. (1983): A model of the OH position in olivine, derived from infrared-

538   spectroscopy investigations. *Phys. Chem. Minerals*, **9**, 57-60.

539   Beran, A. & Libowitzky E. (2006): Water in Natural Mantle Minerals II: Olivine, Garnet and

540   Accessory Minerals. *Rev. Mineral. Geochem.*, **62**, 169-191.

541   Berry, A.J., Hermann, J., O'Neill, H.S.C., Foran, G.J. (2005): Fingerprinting the water site in

542   mantle olivine. *Geology*, **33**, 869-872.

543   Berry, A.J., O'Neill, H.S.C., Hermann, J., Scott, D.R. (2007): The infrared signature of water

544   associated with trivalent cations in olivine. *Earth Planet. Sci. Lett.*, **261**, 134-142.

545   Blanchard, M., Ingrin, J., Kovács I., Withers A.C. (2016): Effect of iron and trivalent cations

546   on OH-defects in olivine. *Am. Mineral.*, (paper with Editor for final decision)

547   Bolfan-Casanova, N. (2005): Water in the Earth's mantle. *Mineral. Mag.*, **69**, 229-257

548   Bolfan-Casanova, N., Montagnac, G., Reynard, B. (2014): Measurement of water contents in

549   olivine using Raman spectroscopy. *Am. Mineral.*, **99**, 149-56.

550   Bonn, M., Brugmans, M.J., Kleyn, A.W., van Santen, R.A., Bakker, H.J. (1996): Vibrational

551   dephasing mechanisms in hydrogen-bonded systems. *Phys. Rev. Lett.*, **76**, 2440-2443.

552   Budde, M., Parks Cheney, C., Lüpke, G., Tolk, N.H., Feldman, L.C. (2001): Vibrational

553   dynamics of bond-center hydrogen in crystalline silicon. *Phys. Rev. B*, **63**, 195203.

554   Chopra, P.N. & Paterson, M.S. (1984): The role of water in the deformation of dunite. *J.*

555   *Geophys. Res.*, **89**, 7861-7876.

556   Crépisson, C., Blanchard, M., Bureau, H., Sanloup, C., Withers, A.C., Khodja, H., Surblé, S.,

557   Béneut, K., Leroy, C., Giura, P., Balan, E. (2014a): Clumped fluoride-hydroxyl

558   defects in forsterite: Implications for the upper-mantle. *Earth Planet. Sci. Lett.*, **390**,

559   287-295.

560   Crépisson, C., Bureau, H., Blanchard, M., Ingrin, J., Balan, E. (2014b): Theoretical infrared

561   spectrum of partially protonated cationic vacancies in forsterite. *Eur. J. Mineral.*, **26**,

562   203-210.

563   Damen, T.C., Porto, S.P.S., Tell, B. (1966): Raman effect in zinc oxide. *Phys Rev*, **142**, 570–

564   574.

565   Demouchy, S., Tommasi, A., Barou, F., Mainprice, D., Cordier, P. (2012): Deformation of

566   olivine in torsion under hydrous conditions. *Phys. Earth Planet. Int.*, 202-203, 57-70.

567   Demouchy, S. & Bolfan-Casanova, N. (2016): Distribution and transport of hydrogen in the

568   lithospheric mantle: A review. *Lithos*, **240-243**, 402-425.

569 Dumas, P., Chabal, Y.J., Higashi, G.S. (1990): Coupling of an adsorbate vibration to a

570   substrate surface phonon: H on Si(111). *Phys. Rev. Lett.*, **65**, 1124-1127.

571 Férot, A. & Bolfan-Casanova, N. (2012): Water storage capacity in olivine and pyroxene to

572   14 GPa: Implications for the water content of the Earth's upper mantle and nature of

573   seismic discontinuities. *Earth Planet. Sci. Lett.*, **349-350**, 218-230.

574 Giannozzi, P., Baroni, S., Bonini, N., Calandra, M., Car, R., Cavazzoni, C., Ceresoli, D.,

575   Chiarotti, G.L., Cococcioni, M., Dabo, I., Dal Corso, A., de Gironcoli, S., Fabris, S.,

576   Fratesi, G., Gebauer, R., Gerstmann, U., Gougoussis, C., Kokalj, A., Lazzeri, M.,

577   Martin-Samos, L., Marzari, N., Mauri, F., Mazzarello, R., Paolini, S., Pasquarello, A.,

578   Paulatto, L., Sbraccia, C., Scandolo, S., Sclauzero, G., Seitsonen, A.P., Smogunov, A.,

579   Umari, P., Wentzcovitch, R.M. (2009): Quantum ESPRESSO: a modular and open-

580   source software project for quantum simulations of materials. *J. Phys.: Condens.*

581   *Matter.*, **21**, 395502.

582 Gose, J., Schmädicke, E., Markowitz, M., Beran, A. (2009): OH point defects in olivine from

583   Pakistan. *Miner. Petrol.*, **99,** 105-111.

584 Grant, K.J., Brooker, R.A., Kohn, S.C., Wood, B.J. (2007): The effect of oxygen fugacity on

585   hydroxyl concentrations and speciation in olivine: Implications for water solubility in

586   the upper mantle. *Earth Planet. Sci. Lett.*, **261**, 219-229.

587 Hushur, A., Manghani, M.H., Smyth, J.R., Nestola, F., Frost, D.J. (2014): Crystal chemistry

588   of hydrous forsterite and its vibrational properties up to 41 GPa. *Am. Mineral.*, **94**,

589   751-760.

590 Ingrin, J., Liu, J., Depecker, C., Kohn, S.C., Balan, E., Grant, K.J. (2013): Low-temperature

591   evolution of OH bands in synthetic forsterite, implication for the nature of H-defects

592   at high pressure. *Phys. Chem. Minerals*, **40**, 499-510.

593   Ingrin, J., Kovács, I., Deloule, E., Balan, E., Blanchard, M., Kohn, S.C., Hermann, J. (2014):

594   Identification of hydrogen defects linked to boron substitution in synthetic forsterite

595   and natural olivine. *Am. Mineral.*, **99**, 2138-2141.

596   Koch-Müller, M., Matsyuk, S.S., Rhede, D., Wirth, R., Khisina, N. (2006): Hydroxyl in

597   mantle olivine xenocrysts from the Udachnaya kimberlite pipe. *Phys. Chem. Minerals*,

598   **33**, 276-287.

599   Koch-Müller, M. & Rhede, D. (2010): IR absorption coefficients for water in nominally

600   anhydrous high-pressure minerals. *Am. Mineral.*, **95**, 770-775

601   Kohlstedt, D.J., Keppler, H., Rubie, D.C. (1996): Solubity of water in the α, β, and γ phases

602   of $(Mg,Fe)_2SiO_4$. *Contrib. Mineral. Petrol.*, **123**, 345-357.

603   Kovács, I., O'Neill, H.St.C., Hermann, J., Hauri, E.H. (2010): Site-specific infrared OH

604   absorption coefficients for water substitution into olivine. *Am. Mineral.*, **95**, 292-299.

605   Kröger, F.A. & Vink, H.J. (1956): Relation between the concentrations of imperfections in

606   crystallines solids. *Sol. State Phys.*, Vol. 3, p. 307. Academy Press, New York.

607   Lazzeri, M., & Mauri, F. (2003): First principles calculation of vibrational Raman spectra in

608   large systems: signature of small rings in crystalline SiO_2. *Phys. Rev. Lett.*, **90**,

609   036401.

610   Lemaire, C., Kohn, S.C., Brooker, R.A. (2004): The effect of silica activity on the

611   incorporation mechanism of water in synthetic forsterite: a polarised infrared

612   spectroscopic study. *Contrib. Mineral. Petrol.*, **147**, 48-57.

613   Li, L, Wentzcovitch, R.M., Weidner, D.J., Da Silva, C.R.S. (2007): Vibrational and

614   thermodynamic properties of forsterite at mantle conditions. *J. Geophys. Res.*, **112**,

615   B05206.

616   Libowitzky, E. & Beran, A. (1995): OH defects in forsterite. *Phys. Chem. Minerals*, **22**, 387-

617   392.

618 _ & _ (2006): The structure of hydrous species in nominally anhydrous minerals: Information

619   from polarized IR spectroscopy. *Rev. Mineral. Geochem.*, **62**, 29-52.

620 Libowitzky, E. & Rossman, G.R. (1997): An IR absorption calibration for water in minerals.

621   *Am. Mineral.*, **82**, 1111-1115.

622 Libowitzky, E. (1999): Correlation of OH stretching frequencies and O-H...O hydrogen bond

623   length in minerals. *Mh. Chem.*, **130**, 1047-1059.

624 Mackwell, S.J., Kohlstedt, D.L., Paterson, M.S. (1985): The role of water in the deformation

625   of olivine single crystals. *J. Geophys. Res.*, **90**, 11319-11333.

626 Martin, K.R., Blaney, P., Shi, G., Stavola, M., Fowler, W.B. (2006): Temperature dependence

627   of the vibrational spectrum of a Li-OH complex in ZnO: Infrared absorption

628   experiments and theory. *Phys Rev B*, **73**, 232509.

629 Matsyuk, S.S. & Langer, K. (2004): Hydroxyl in olivines from mantle xenoliths in

630   kimberlites of the Siberian platform. *Contrib. Mineral. Petrol.*, **147**, 413-437.

631 Matveev, S., O'Neill H.St.C., Ballhaus, C., Taylor, W.R., Green, D.H. (2001): Effect of silica

632   activity on OH-IR spectra of olivine: implications for low-$aSiO_2$ mantle

633   metasomatism. *J. Petrol.*, **42**, 721-729.

634 Matveev, S., Portnyagin, M., Ballhaus, C., Brooker, R.A., Geiger, C.A. (2005): FTIRS

635   spectrum of phenocryst olivine as an indicator of silica saturation in magmas. *J.*

636   *Petrol.*, **46**, 605-614.

637 Matveev, S. & Stachel T. (2009): Evaluation of kimberlite diamond potential using FTIR

638   spectroscopy of xenocrystic olivine. *Lithos*, **112**, 36-40.

639 Mei, S. & Kohlstedt, D.L. (2000): Influence of water on plastic deformation of olivine

640   aggregates 2. Dislocation creep regime. *J. Geophys. Res.*, **105**, 21471-21481.

641 Mosenfelder, J.L., Deligne, N.I., Asimow, P.D., Rossman, G.R. (2006): Hydrogen

642   incorporation in olivine from 2-12 GPa. *Am. Mineral.*, **91**, 285-294.

643   Nakamoto, K., Margosches, M., Rundle, R.E. (1955): Stretching frequencies as a function of

644   distances in hydrogen bonds. *J. Am. Chem. Soc.*, **77**, 831–857.

645   Nakamura, A. & Schmalzried, H. (1983): On the nonstoichiometry and point defects of

646   olivine. *Phys. Chem. Minerals*, **10**, 27-37.

647   Paterson, M.S. (1982): The determination of hydroxyl by infrared absorption in quartz,

648   silicate glasses and similar materials. *Bull. Minéral.*, **105**, 20-29.

649   Perdew, J.P., Burke, K., Ernzerhof, M. (1996): Generalized Gradient Approximation Made

650   Simple. *Phys. Rev. Lett.*, **77**, 3865–3868.

651   Persson, B.N.J. & Ryberg, R. (1985a): Vibrational phase relaxation at surfaces: CO on

652   Ni(111). *Phys. Rev. Lett.*, **54**, 2119-2122.

653   _ & _ (1985b): Brownian motion and vibrational phase relaxation at surfaces: CO on Ni(111).

654   *Phys Rev B*, **32**, 3586-3596.

655   Prechtel, F. & Stalder, R. (2011): The potential use of OH-defects in enstatite as

656   geobarometer. *Contrib. Mineral. Petrol.*, **162**, 615-623.

657   Rao, K., S.L. Chaplot, N. Choudury, S. Ghose, J.M. Hastings, L.M. Corliss (1988): Lattice

658   dynamics and inelastic neutron scattering from forsterite, Mg_2SiO_4: phonon dispersion

659   relation, density of states, and specific heat. *Phys. Chem. Minerals*, **16**, 83-97.

660   Smyth, J.R., Frost, D.J., Nestola, F., Holl, C.M., Bromiley, G. (2006): Olivine hydration in

661   the deep upper mantle: effects of temperature and silica activity. *Geophys. Res. Lett.*,

662   **33,** L15301.

663   Szalay, V., Kovács, L., Wöhlecke, M., Libowitzky, E. (2002): Stretching potential and

664   equilibrium length of the OH bonds in solids. *Chem. Phys. Lett.*, **354**, 56-61.

665   Tasaka, M., Zimmeramn, M.E., Kohlstedt., D.L. (2015): Creep behavior of Fe-bearing olivine

666   under hydrous conditions. *J. Geophys. Res.*, **120**, 6039-6057.

667 Umemoto, K., Wentzcovitch, R.M., Hirschmann, M.M., Kohlstedt, D.L., Withers, A.C.

668   (2011): A first-principles investigation of hydrous defects and IR frequencies in

669   forsterite: The case for Si vacancies. *Am. Mineral.*, **96**, 1475-1479.

670 Walker, A.M., Demouchy, S., Wright, K. (2006): Computer modelling of the energies and

671   vibrational properties of hydroxyl groups in α- and β-Mg_2SiO_4. *Eur. J. Mineral.*, **18**,

672   529-543.

673 Walker, A.M., Hermann, J., Berry, A.J., O'Neill, H.St.C. (2007): Three water sites in upper

674   mantle olivine and the role of titanium in the water weakening mechanism. *J. Geophy.*

675   *Res.*, **112**, B05211.

676 Wilkins, R.W.T. & Sabine, W. (1973): Water content of some nominally anhydrous silicates.

677   *Am. Mineral.*, **58**, 508-516.

678 Withers, A.C., Hirschmann, M.M., Tenner T.J. (2011): The effect of Fe on olivine H_2O

679   storage capacity: Consequences for H_2O in the martian mantle. *Am. Mineral.*, **96**,

680   1039-1053.

681 Withers, A.C., Bureau, H., Raepsaet, C., Hirschmann, M.M. (2012): Calibration of infrared

682   spectroscopy by elastic recoil detection analysis of H in synthetic olivine. *Chem.*

683   *Geol.*, **334**, 92–98.

684 Wood, P.A., Allen, F.H., Pidcock, E. (2009): Hydrogen-bond directionality at the donor H

685   atom—analysis of interaction energies and database statistics. *CrystEngComm*, **11**,

686   1563-1571.

687 Xue, X., Kanzaki, M., Turner, D., Loroch, D. (2016): Hydrogen incorporation mechanisms in

688   forsterite: ^{1}H NMR measurement and first- principles calculation. *Goldschmidt*

689   *Conference Abstracts* 3503.

690 Yang, X. & Keppler, H. (2011): In-situ infrared spectra of OH in olivine to 1100℃. *Am.*

691   *Mineral.*, **96**, 451-454.

692

693

694
695

Figure captions:

697

698   Figure 1: (a) Experimental infrared spectrum of hydrous forsterite at low temperature (Ingrin

699   *et al*. 2013). Individual contributions obtained from spectral decomposition have been shifted

700   for clarity. The bands 3a and 8a represent 14% and 23% of the total absorbance, respectively.

701   (b) Wavenumber of bands 3a, 7a and 8a as a function of temperature. The full lines

702   correspond to constrained fits using Eq. 1 (see text). (c) Full-width at half maximum of bands

703   3a, 7a and 8a as a function of temperature. The lines correspond to the model behaviour

704   determined from the fits of Fig. 1a and 1d. (d) $\ln(\Delta\Gamma/(\Delta\Omega)^2)$ as a function of T^{-1}. The point at

705   79K has not been included in the linear fit of band 3a and 8a. The behaviour of bands 4a, 5a

706   and 7a is reported for comparison .

707

708

709   Figure 2: Models of protonated cationic vacancies in forsterite. The B_H_1 model

710   corresponds to the most stable configuration of the clumped $(B, H)_{Si}^{x}$ defect reported by Ingrin

711   *et al*. (2014). The Si_3 model corresponds to the most stable configuration of the $(4H)_{Si}^{x}$

712   defect reported by Balan *et al*. (2011). The O2-H environment is similar in both defects. The

713   O3-H and O1-H in the Si_3 models share weak H-bonds with nearby OH groups. (note:

714   X=[100]=γ, Y=[010]=α and Z=[001]=β)

715

716   Figure 3: Theoretical polarized Raman spectra of hydrous forsterite modeled using a

717   lorentzian broadening of 3 cm^{-1}. Spectra are described using the Porto notation, $k_i(E_iE_s)k_s$,

718   where the two symbols inside the parenthesis are the polarization of the incident and scattered

719   light, while the ones outside are, from left to right, the propagation directions of the incident

720   and scattered light, respectively (Damen *et al*., 1966). Band positions are specified in cm^{-1}.

721   The inset shows the room temperature experimental Raman spectrum of sample 691 from

722   Bolfan-Casanova *et al.* (2014). The correspondence with the bands 7a, 5a and 3a identified in

723   the infrared spectra is indicated. The band at 3480 cm^{-1} corresponds to a different

724   configuration of $(4H)_{Si}^x$ defect (Balan *et al.*, 2011).

725

726   Figure 4: Scheme of hydrogen cartesian displacements for the stretching modes of the Si_3

727   model of $(4H)_{Si}^x$ defect. The displacement vectors have been obtained from the corresponding

728   eigenvectors of the dynamical matrix and the theoretical frequency is reported. Experimental

729   band labelling and room temperature frequency are reported in parenthesis.

730

731   Figure 5: Potential energy surface determined for longitudinal δx and transverse δz

732   displacements of the H atom in the B_H_1 model of $(B,H)_{Si}^x$ defect. Note the peculiar shape

733   of the potential. The spatial extension of atomic displacements is consistent with the ground

734   state delocalization of the H atom (Table 2).

735

736   Figure 6: Potential energy curves corresponding to sections of the potential energy surface

737   along the longitudinal and transverse directions for the O2-H and O1-H groups.

738

739   Figure 7: Theoretical frequencies of hindered translation (short vertical bars) and rotation

740   (long vertical bars) modes of OH groups obtained from partial dynamical matrix. The shaded

741   areas are covered by the phonon density of states of forsterite (Li *et al.*, 2007). The peculiar

742   anharmonic properties of O2-H groups are ascribed to their significant interaction with the

743   vibrations of the crystal through hindered rotation modes.

744

745   Table 1: Spectroscopic and mode-coupling parameters obtained from experimental data

band	ω_0 (cm^{-1})	Γ_0 (cm^{-1})	ω_{ex} (cm^{-1})	$\delta\omega$ (cm^{-1})	η (cm^{-1})
3a	3566.2	4.8	387	-68	137
8a	3617.2	4.4	470	-142	438

746

747

748
749
750
751
752
753
754
755

756
757

Table 2: Coefficients of the polynomial fit of potential energy surfaces for longitudinal δx and transverse δz displacements. The corresponding polynomial function is $E(x,z)= a\ (\delta x)^2 + b\ (\delta x)^3 + c\ (\delta x)^4 + d\ (\delta z)^2 + e\ (\delta z)^2(\delta x) + f\ (\delta z)^2(\delta x)^2 + g\ (\delta z)^2(\delta x)^3 + h\ (\delta z)^2(\delta x)^4 + i\ (\delta z)^4 + j\ (\delta z)^4(\delta x) + k\ (\delta z)^4(\delta x)^2$, where the energy is in Rydberg and the displacements in atomic units (a_0). Note that terms related to odd powers of (δz) are zero because of the system symmetry.

coefficient	displacements	std. error	B_H_1	Si_3 (O2-H)	Si_3 (O1-H)
a	$(\delta x)^2$	+/- 0.001	0.471	0.459	0.459
b	$(\delta x)^3$	+/- 0.001	-0.581	-0.571	-0.587
c	$(\delta x)^4$	+/- 0.006	0.396	0.391	0.396
d	$(\delta z)^2$	+/- 0.001	0.008	0.008	0.016
e	$(\delta z)^2(\delta x)$	+/- 0.003	0.243	0.239	0.255
f	$(\delta z)^2(\delta x)^2$	+/- 0.02	-0.589	-0.578	-0.587
g	$(\delta z)^2(\delta x)^3$	+/- 0.01	0.658	0.644	0.658
h	$(\delta z)^2(\delta x)^4$	+/- 0.08	-0.603	-0.589	-0.605
i	$(\delta z)^4$	+/- 0.01	0.025	0.025	0.024
j	$(\delta z)^4(\delta x)$	+/- 0.02	-0.249	-0.244	-0.250
k	$(\delta z)^4(\delta x)^2$	+/- 0.08	0.449	0.438	0.449

758
759
760
761
762
763

764   Table 3: Harmonic theoretical properties of transverse (δx=0) and longitudinal (δz=0) OH
765   vibrational modes
766
767

	model	quadratic coefficient (Ry/a$_0^2$)	frequency (H) (cm^{-1})	frequency (H DM) (cm^{-1})	frequency (OH DM) (cm^{-1})	frequency (full DM) (cm^{-1})	σ (a$_0$)
δx=0	B_H_1	0.008	472	450	510	-	0.25
	Si_3 (O2-H)	0.008	450	437	497	-	0.25
	Si_3 (O1-H)	0.016	645	631	638	-	0.21
δz=0	B_H_1	0.471	3513	3518	3618	3618	0.09
	Si_3 (O2-H)	0.459	3470	3474	3574	3573	0.09
	Si_3 (O1-H)	0.458	3467	3471	3578	3592	0.09
	Si_3 (O3-H)	-	-	3434	3536	3540, 3520	-

768
769   Notes: harmonic frequencies are obtained from the quadratic polynomial coefficient of
770   potential energy and motion of H atom only (H); the partial dynamical matrix restricted to H
771   atom (H DM); the partial dynamical matrix restricted to OH group (OH DM); and the full
772   dynamical matrix (full DM). The minor differences with previous studies (Balan *et al*., 2011;
773   Ingrin *et al*., 2014) are related to the more stringent convergence criteria imposed on the
774   forces for the defect relaxation. Note that the full dynamical matrix does not enable a clear

775   identification of transverse modes. The standard deviation of the modes $\sigma = \sqrt{\dfrac{h}{4\pi m \omega}}$ is

776   obtained from the quadratic polynomial coefficient of potential energy and motion of H atom
777   only. It reflects the ground-state delocalization of the H atom.
778

Figure 1

Figure 2

$(B,H)^x_{Si}$ defect

B_H_1 model

$(4H)^x_{Si}$ defect

Si_3 model
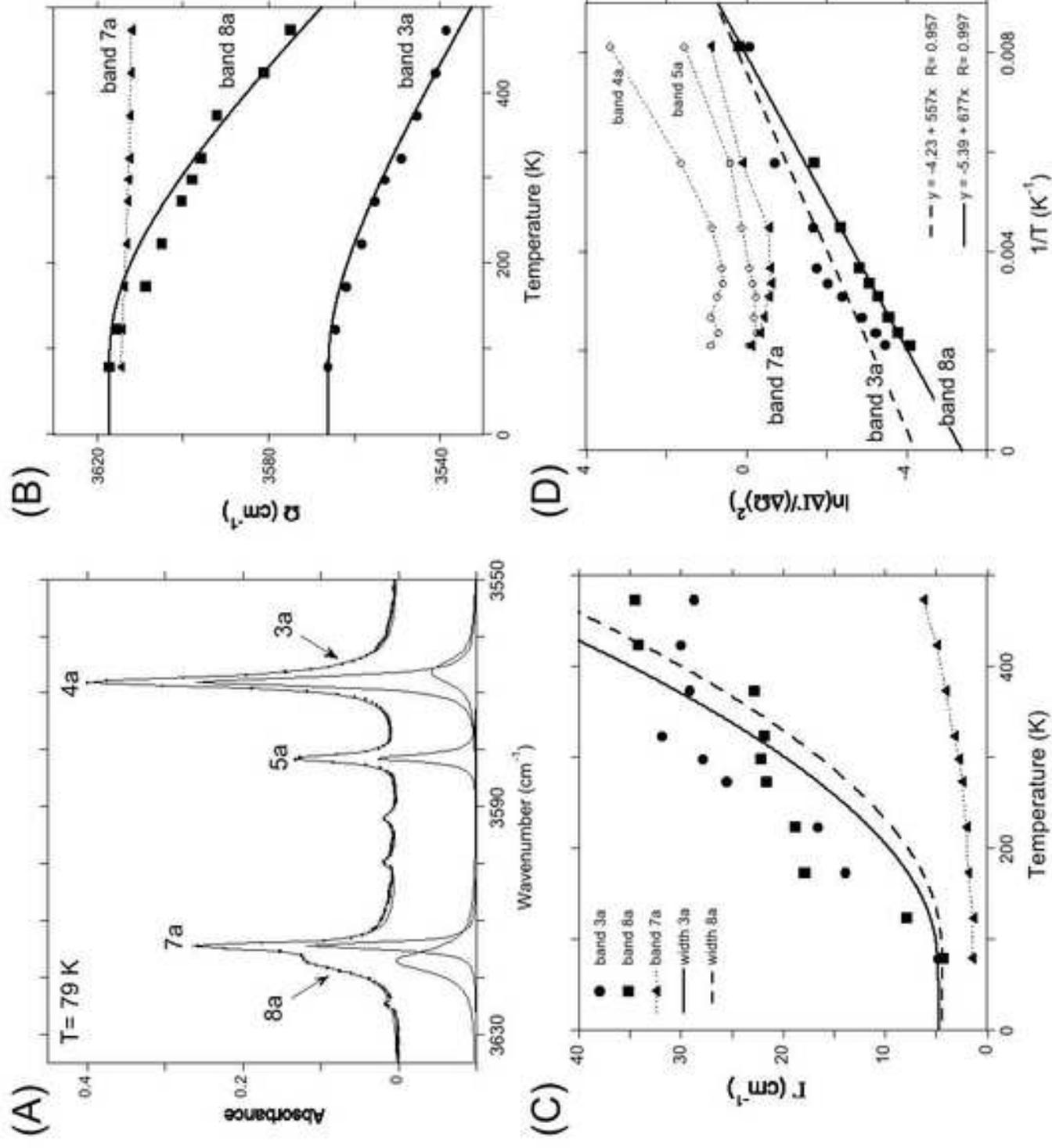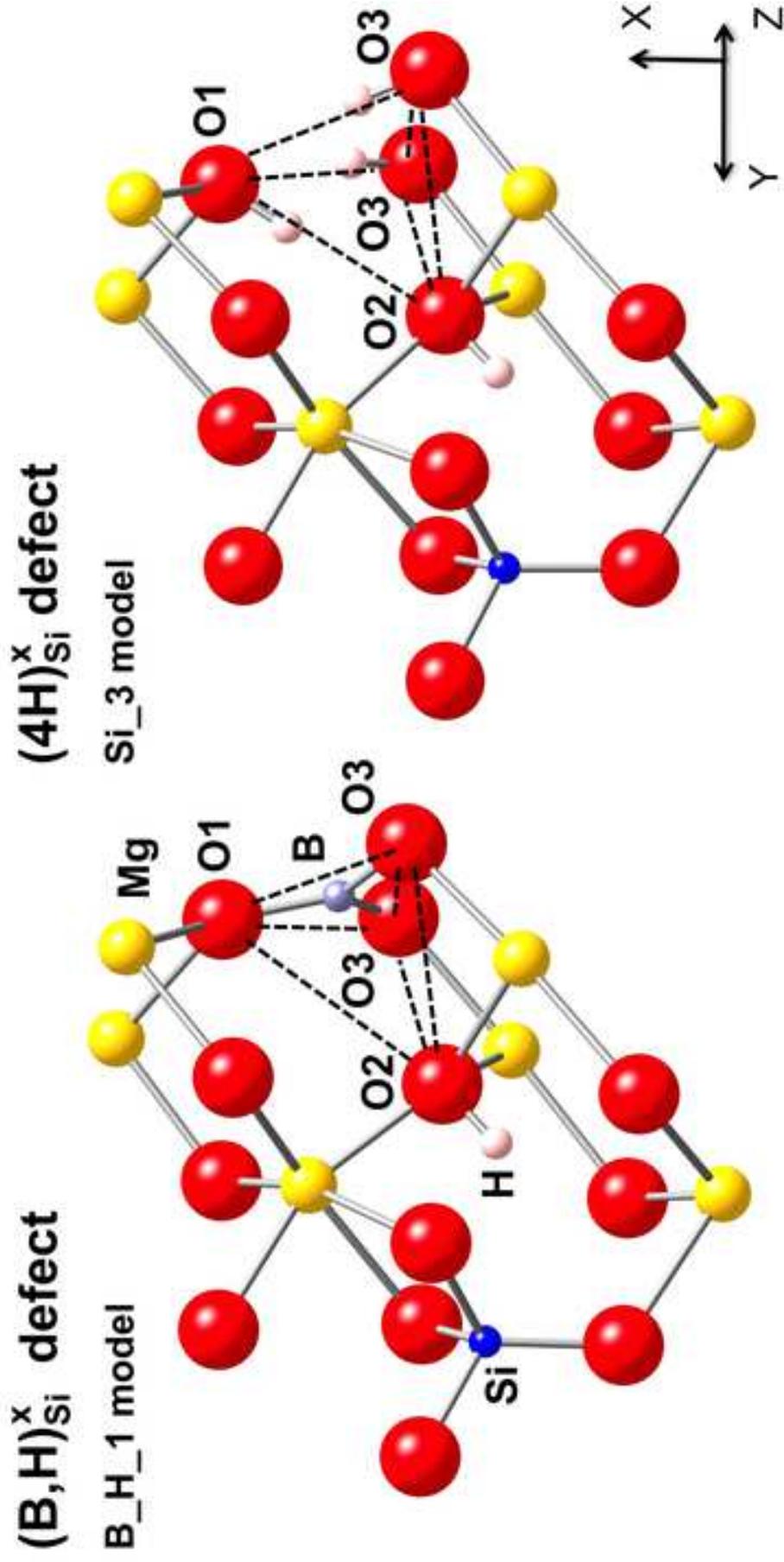
Figure 3

Click here to download Figure Fig3.jpg

Figure 3

Figure 4

3592 cm⁻¹
(7a, 3613 cm⁻¹)

3573 cm⁻¹
(3a, 3550 cm⁻¹)

3540 cm⁻¹
(5a, 3580 cm⁻¹)

3520 cm⁻¹
(4a, 3567cm⁻¹)

Figure 5

B_H_1

Figure 6

Figure 7